

The CARMENES search for exoplanets around M dwarfs

A homogeneous catalogue of projected rotational velocities accounting for limb darkening

R. Varas^{1,*}, G. Morello^{1,2}, M. Zechmeister³, P. J. Amado¹, F. J. Pozuelos¹, J. A. Caballero⁴, A. Claret^{1,5}, C. Cifuentes⁴, R. Morales¹, A. Quirrenbach⁶, A. Reiners³, I. Ribas^{7,8}, V. J. S. Béjar^{9,10}, M. Cortés-Contreras¹¹, A. P. Hatzes¹², Th. Henning¹³, I. Hermelo¹⁴, H. L. Ruh³, A. Schweitzer¹⁵, H. M. Tabernero^{7,8}, and M. R. Zapatero Osorio⁴

¹ Instituto de Astrofísica de Andalucía, CSIC, Glorieta de la Astronomía s/n, 18008 Granada, Spain

² INAF – Palermo Astronomical Observatory, Piazza del Parlamento, 1, 90134 Palermo, Italy

³ Institut für Astrophysik und Geophysik, Georg-August-Universität Göttingen, Friedrich-Hund-Platz 1, 37077 Göttingen, Germany

⁴ Centro de Astrobiología, CSIC-INTA, Camino Bajo del Castillo s/n, Campus ESAC, 28692 Villanueva de la Cañada, Madrid, Spain

⁵ Universidad de Granada, c/ Gran Vía de Colón 48, 18010 Granada, Spain

⁶ Landessternwarte, Zentrum für Astronomie der Universität Heidelberg, Königstuhl 12, 69117 Heidelberg, Germany

⁷ Institut de Ciències de l’Espai, CSIC, c/ de Can Magrans s/n, Campus UAB, 08193 Bellaterra, Barcelona, Spain

⁸ Institut d’Estudis Espacials de Catalunya, 08860 Castelldefels, Barcelona, Spain

⁹ Instituto de Astrofísica de Canarias, 38205 La Laguna, Tenerife, Spain

¹⁰ Departamento de Astrofísica, Universidad de La Laguna, 38206 La Laguna, Tenerife, Spain

¹¹ Departamento de Física de la Tierra y Astrofísica & IPARCOS Instituto de Física de Partículas y del Cosmos, Facultad de Ciencias Físicas, Universidad Complutense de Madrid, Plaza de Ciencias 1, 28400 Madrid, Spain

¹² Thüringer Landessternwarte Tautenburg, Sternwarte 5, 07778 Tautenburg, Germany

¹³ Max-Planck-Institut für Astronomie, Königstuhl 17, 69117 Heidelberg, Germany

¹⁴ Centro Astronómico Hispano en Andalucía, Observatorio Astronómico de Calar Alto, Sierra de los Filabres, 04550 Gérgal, Almería, Spain

¹⁵ Hamburger Sternwarte, Gojenbergsweg 112, 21029 Hamburg, Germany

Received 28 January 2026 / Accepted 10 April 2026

ABSTRACT

Stellar rotation is closely linked to both the age and the magnetic activity of stars. Through gyrochronology, studying stellar rotation provides a means to estimate stellar ages and trace the evolution of planetary systems, and it is also a crucial means to constrain and correct stellar activity effects for robust exoplanet detection and characterisation. CARMENES is a dual-channel, high-resolution ($\mathcal{R} > 80\,000$) spectrograph that has been highly successful in detecting exoplanets around M-dwarf stars using the radial-velocity technique, and it also enables precise measurements of the projected rotational velocity ($v \sin i$) from spectral line broadening. We present an oversampled convolution method that incorporates a realistic limb-darkening model to determine $v \sin i$ from CARMENES spectra by comparing observed spectra with that of a template star. The advantages over existing methods in the literature have been assessed using high-resolution synthetic spectra that span effective temperatures of 2500–4000 K and projected rotational velocities of up to 50 km s^{-1} . We applied our method to 392 M dwarfs observed with CARMENES and it yielded $v \sin i$ measurements (or upper limits at 2 km s^{-1}) with a median relative uncertainty of 6.8%, which is substantially smaller than the 15.4% reported in the literature. This work provides the largest uniform catalogue of $v \sin i$ measurements for M dwarfs, including significantly updated values for several targets, along with 36 new targets.

Key words. methods: numerical – techniques: spectroscopic – stars: activity – stars: late-type – stars: rotation

1. Introduction

M-dwarf stars are the most numerous stellar population in our Galaxy, constituting roughly 75% of stars in the solar neighbourhood (Henry et al. 2006, 2018). Their small sizes and masses ($0.61\text{--}0.075 M_{\odot}$; Henry & Jao 2024), low temperatures (3900–2300 K; Cifuentes et al. 2020), and long lifetimes make them prime targets for the detection of small, temperate exoplanets (Bonfils et al. 2013; Sabotta et al. 2021). Characterising the rotation of M dwarfs provides information about their magnetic

activity, internal structure, and age (Suárez Mascareño et al. 2015; Newton et al. 2016; Díez Alonso et al. 2019; Shan et al. 2024). These constraints are essential for interpreting the formation and evolution of their planetary systems.

The Calar Alto high-Resolution search for M dwarfs with Exoearths using Near-infrared and optical Echelle Spectrographs (CARMENES¹) project provides an excellent dataset for improving rotational velocity measurements in M dwarfs. CARMENES is a dual-channel spectrograph (VIS: 520–960 nm; NIR: 960–1710 nm) with a high spectral resolution ($\mathcal{R} = 94\,600$

* Corresponding author: rvaras@iaa.es

¹ <https://carmenes.caha.es>

and $\mathcal{R}=80\,400$, respectively), mounted on the 3.5 m telescope at the Calar Alto Observatory (CAHA) in Almería, Spain (Quirrenbach et al. 2014, 2018). The survey has delivered high-quality spectra and radial-velocity (RV) time series for nearly 400 nearby M dwarfs (Ribas et al. 2023), which has enabled the discovery of numerous exoplanets as well as detailed studies of stellar rotation, activity, and variability (Baroch et al. 2020; Jeffers et al. 2022; Fuhrmeister et al. 2018, 2023; Shan et al. 2024; Ruh et al. 2024).

A fundamental measure of stellar rotation is the projected rotational velocity, $v \sin i$, which represents a star’s equatorial rotation along the line of sight. It is typically inferred from the Doppler broadening of absorption lines in high-resolution spectra. Determining $v \sin i$ accurately is challenging, as rotational broadening must be disentangled from other line-broadening mechanisms, such as instrumental effects and stellar turbulence. Conventional approaches often approximate the rotational profile using a convolution kernel that accounts for limb darkening. However, most studies adopt a fixed linear limb-darkening coefficient (usually $u=0.6$) that is independent of spectral type or wavelength (Jenkins et al. 2009; Reiners et al. 2012, 2022). As demonstrated in this work, this simplification can lead to systematic biases.

Our approach introduces two key enhancements to modelling rotational broadening. First, we applied an oversampled convolution to minimise numerical artefacts. Second, we adopted order-specific limb-darkened kernels that account for wavelength- and temperature-dependent linear coefficients. For each target and spectral order, we computed average u values from stellar-atmosphere models and achieved higher fidelity across the full wavelength range. Tests based on synthetic spectra indicate that this method improves both the precision and accuracy of the results, while remaining computationally efficient.

We applied this method to 392 M dwarfs with CARMENES-VIS observations, which enabled us to make a direct comparison with previous studies based solely on VIS data. This application yielded a homogeneous catalogue² of $v \sin i$ measurements. In Appendix A we discuss the prospects for extending the method to CARMENES-NIR data.

2. Observations and data reduction

2.1. CARMENES spectra

The CARMENES spectra were reduced using the *caracal* (CARMENES Reduction And CALibration) pipeline, as detailed by Caballero et al. (2016). Starting with the raw data, *caracal* performs dark and bias correction, order tracing, flat-relative optimal extraction, and wavelength calibration, which results in fully reduced and wavelength-calibrated 1D spectra.

The second pipeline is *serval* (SpEctrum Radial Velocity AnaLyser, Zechmeister et al. 2018). It creates a high signal-to-noise ratio spectrum using the reduced spectra of the target star. It then computes the series of RVs via least-square fitting, telluric masking, échelle order weighting, and correcting for systematic effects. The output also includes activity indices. Here we present the implementation in *serval* of the computation of the $v \sin i$ accounting for the effect of limb darkening.

2.2. Synthetic data

We adopted four spectra from the PHOENIX NewEra stellar atmosphere models (Hauschildt et al. 2025) and corresponding

² <https://github.com/rvarasg/vsini-limb-darkening>

surface intensity distributions (Claret et al. 2025). The synthetic templates were selected from among main-sequence stars with solar metallicity, covering the range $T_{\text{eff}} = 2500\text{--}4000$ K in steps of 500 K. Each template provides intensity spectra at 127 μ values, where μ is the cosine of the angle between the normal to the stellar surface and the line of sight, spanning the wavelength range 1000–60 000 Å with a constant step of 0.05 Å. These model spectra fully cover the CARMENES wavelength range at a slightly higher sampling rate than the instrument.

We numerically integrated the stellar spectrum over a grid of 3000×3000 square cells covering the sky-projected stellar disc, following the method described by Morello et al. (2022) and Canocchi et al. (2024). Each cell is identified by the Cartesian coordinates of its centre (x_j, y_j) , which are normalized to the stellar radius. The corresponding μ_j values are calculated as

$$\mu_j = \sqrt{1 - x_j^2 - y_j^2}. \quad (1)$$

The ‘static’ cell spectrum is then obtained by interpolation at μ_j from the template, here using a cubic spline, though the method is only weakly sensitive to the choice of interpolation scheme. To account for stellar rotation, we Doppler-shifted the spectrum of each cell according to its velocity along the line of sight,

$$v_j = (y_j \sin \bar{\lambda} - x_j \cos \bar{\lambda}) \cdot v \sin i, \quad (2)$$

where $\bar{\lambda}$ is a dummy parameter in this context (we set $\bar{\lambda}=0$). In the presence of a transiting planet, $\bar{\lambda}$ traditionally denotes the sky-projected spin-orbit angle. We resampled the Doppler-shifted spectra onto the same wavelength grid as the template through linear interpolation, allowing for the direct summation of the cell spectra.

3. Methods

The rotational broadening of stellar spectra can be implemented using several approaches. The two most common ones are convolution with a rotational broadening kernel (Gray 2005) and direct numerical integration (Carvalho & Johns-Krull 2023). Although numerical integration provides a more general and potentially more accurate procedure, it is computationally more expensive. These methods are often adopted with a single linear limb-darkening coefficient (commonly $u = 0.6$), despite the fact that u depends on both stellar temperature and wavelength. In this work, we develop an oversampled convolution method that offers a fast and robust alternative while properly accounting for wavelength- and temperature-dependent limb darkening.

The following subsections describe the method and the incremental improvements, tested using synthetic spectra, that guided its development. The test setup consists of a disc-integrated reference spectrum with $v \sin i = 0 \text{ km s}^{-1}$ and a rotationally broadened target spectrum with $v \sin i$ values of 4, 8, 14, 20, 30, and 50 km s^{-1} , and effective temperatures of $T_{\text{eff}} = 2500, 3000, 3500,$ and 4000 K. These values are representative of the M-dwarf sample observed by CARMENES, although the method itself does not, in principle, impose any restriction on the stellar parameters. For each case, $v \sin i$ was computed using the linear limb-darkening law with theoretical u coefficients.

3.1. Classic convolution and grid-based $v \sin i$ fitting

The standard approach to determining $v \sin i$ involves convolving a chosen template spectrum with a rotational broadening kernel

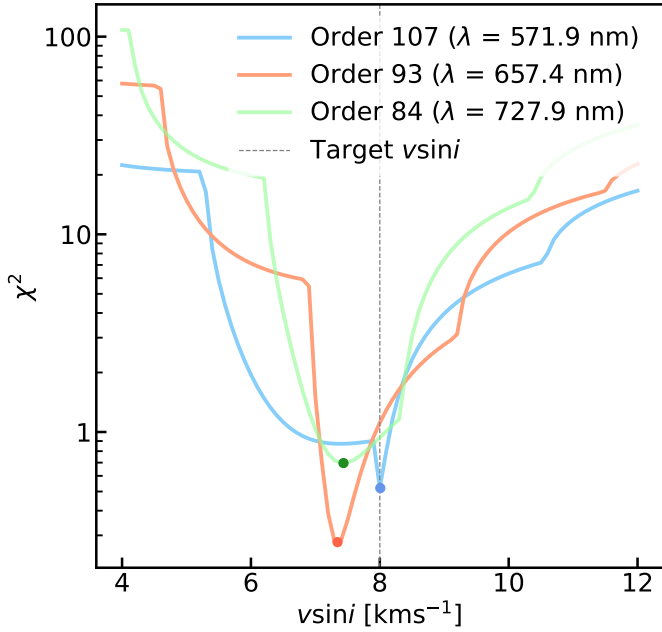


Fig. 1. χ^2 minimization between reference and target synthetic spectra as a function of $v \sin i$ for three spectral orders, computed without limb-darkening correction. The spectra correspond to $T_{\text{eff}} = 3000$ K, with a target value of $v \sin i = 8 \text{ km s}^{-1}$ (vertical line).

over a grid of trial $v \sin i$ values, and minimising the residuals with respect to the target spectrum. In this work, we adopted the commonly used semi-circular kernel, which represents a rigidly rotating, uniformly emitting stellar disc:

$$\tilde{K}(\tilde{v}) = \sqrt{1 - \tilde{v}^2}, \quad (3)$$

where \tilde{v} is the velocity normalised to $v \sin i$. The kernel was subsequently normalised to conserve flux.

We generated a set of broadened templates by convolving the reference spectrum with the kernel over a grid of $v \sin i$ values with steps of $\Delta(v \sin i) = 0.01 \text{ km s}^{-1}$. Both the target and template spectra were cubic-interpolated onto the CARMENES wavelength grid, which has an approximately constant spectral resolution and therefore corresponds to a uniform sampling in $\ln \lambda$. We compared each broadened template with the target spectrum, and the optimal $v \sin i$ was obtained through χ^2 minimization, defined as

$$\chi^2(v \sin i) = \sum_i \left(\frac{f_i - f_{\text{tpl}}(\lambda_i, v \sin i)}{\sigma_i} \right)^2, \quad (4)$$

where f_i and $f_{\text{tpl}}(\lambda_i, v \sin i)$ are the target and the artificially broadened template fluxes, respectively, and σ_i is the target flux uncertainty. We then fitted a parabola to the χ^2 values at the minimum and its two adjacent grid points, and the vertex was adopted as the final $v \sin i$. This procedure was applied independently to each corresponding CARMENES-VIS échelle order (108–66, 562.3–934.3 nm). The final $v \sin i$ for a given target is taken as the median of the order-by-order estimates, while the standard deviation provides the uncertainty.

Figure 1 illustrates the χ^2 minimization as a function of $v \sin i$ for three spectral orders. The resulting $v \sin i$ is indicated by a circular marker. These curves exhibit kinks at different $v \sin i$

values, which bias the inferred velocity depending on their proximity to the true solution. The origin of these kinks is explained in the following subsection.

3.2. Oversampling

The numerical discretisation of the kernel in Eq. (3) naturally leads to small kinks when varying $v \sin i$, because the kernel is evaluated on a discrete logarithmic wavelength grid. The velocity sampling is fixed by $\Delta v = \Delta(\ln \lambda) c$, so that the theoretical kernel half-width is

$$k_{\text{max}} = \frac{v}{\Delta v}. \quad (5)$$

In practice the convolution uses the integer quantity

$$k = \lfloor k_{\text{max}} \rfloor, \quad (6)$$

which is the number of grid points effectively included in the discrete kernel. The discretised rotational kernel is then computed as

$$\tilde{K}(j) = \sqrt{1 - \left(\frac{j}{k_{\text{max}}} \right)^2}, \quad j = -k, \dots, k, \quad (7)$$

and the convolution is performed on the same logarithmic wavelength grid. Each time $v \sin i$ increases enough for k_{max} to cross an integer boundary, the kernel jumps from $k(v_0)$ to $k(v_1) = k(v_0) + 1$, producing a step-wise change that propagates into the χ^2 curve and may shift the position of the minimum.

To mitigate this effect, we oversampled the template spectrum before the convolution. The template spectrum was interpolated (first-order spline) onto a finer grid, convolved with the rotational kernel for the desired $v \sin i$, and then downsampled back to the native wavelength points for the computation of residuals. This approach preserves the original sampling while smoothing the discontinuities introduced by the discrete kernel. The oversampling factor scales linearly with the wavelength grid density, hence, with a factor of N the wavelength grid contains N -times more sampling points. Note that factor = 1 means no oversampling is applied.

Figure 2 illustrates how increasing the oversampling factor reduces the amplitude of the discontinuities. Figure 3 shows the resulting $v \sin i$ estimates for each spectral order. Oversampling substantially improves the consistency of $v \sin i$ estimates across the wavelength. Increasing the factor from 1 to 3 reduces the scatter by $\sim 50\%$. Larger factors do not yield any significant additional gain, with median values and uncertainties essentially unchanged. We therefore adopted an oversampling factor of 5 as an efficient compromise between computational cost and precision.

3.3. Limb darkening

We hypothesise that the remaining discrepancies in our analysis (offsets and trends) may be related to stellar limb darkening, which modifies the rotational broadening kernel through the non-uniform surface brightness of the stellar disc. The general form of the limb-darkened rotational kernel is given in Appendix B (Eq. (B.1)).

For a circularly symmetric disc, $\mu = \sqrt{1 - r^2}$, where r is the projected radial coordinate normalised to a reference radius. Several functional forms have been proposed to approximate $I_i(\mu)$;

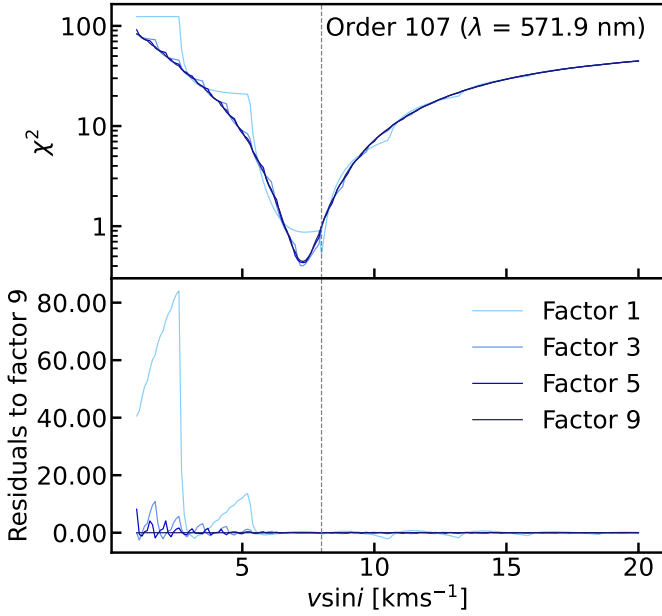


Fig. 2. Top: χ^2 minimization as a function of $v \sin i$ for different oversampling factors. Bottom: residuals relative to the best-fit solution (oversampling factor=9). The convolution kernel does not include any limb-darkening effect. The vertical line marks the target value $v \sin i = 8 \text{ km s}^{-1}$, obtained from synthetic spectra with $T_{\text{eff}} = 3000 \text{ K}$.

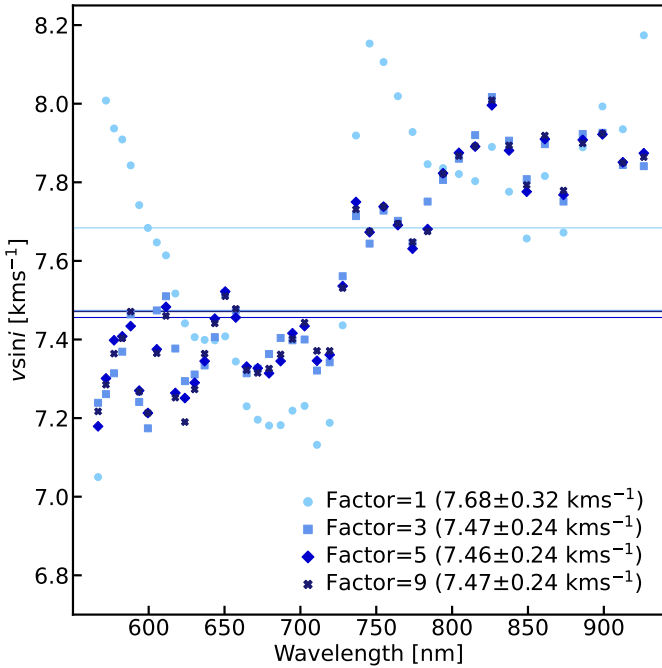


Fig. 3. Best-fitting $v \sin i$ values as a function of wavelength for different oversampling factors, obtained without accounting for limb-darkening in the convolution process. Horizontal lines correspond to the median values. The spectra correspond to $T_{\text{eff}} = 3000 \text{ K}$ and a target value of $v \sin i = 8 \text{ km s}^{-1}$.

the mathematical derivation of the kernels, including the effect of limb darkening, is described in Appendix B. In this work, we find that the linear law (Milne 1921) provides sufficient precision. More complex prescriptions, such as the power-2 law (Hestroffer 1997; Morello et al. 2017), yield improvements below 0.5% (see Appendix C).

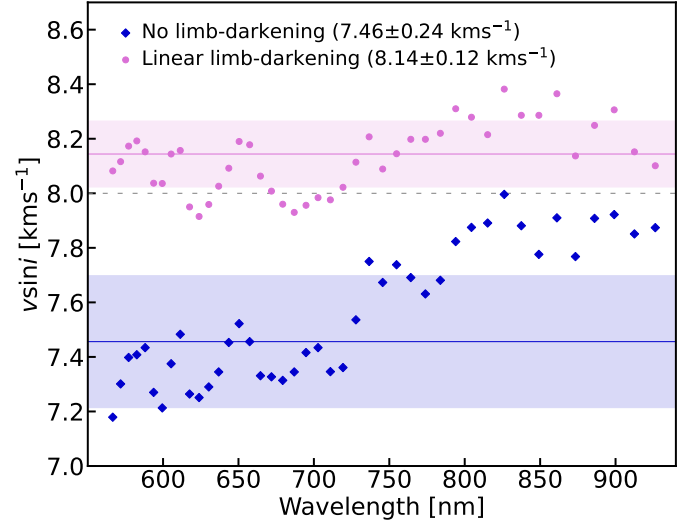


Fig. 4. Best-fitting $v \sin i$ values as a function of wavelength, obtained with and without accounting for limb darkening during the convolution. Horizontal solid lines indicate the median values, and the shaded regions represent the standard deviations. The dashed line marks the target value $v \sin i = 8 \text{ km s}^{-1}$ for spectra with $T_{\text{eff}} = 3000 \text{ K}$.

The normalised kernel for a linear limb-darkening law in Eq. (B.9) can be written in a discrete form as

$$\tilde{K}(x) = \frac{2(1-u)\sqrt{1-x^2} + \frac{\pi}{2}u(1-x^2)}{\pi(1-\frac{u}{3})}, \quad (8)$$

where $x = j/k_{\text{max}}$ and u is the limb-darkening coefficient.

However, because limb darkening varies with wavelength, a single coefficient cannot reproduce the stellar intensity profile accurately across all spectral orders. To account for this wavelength dependence, we determined an optimal coefficient for each spectral order. The simplest approach consists of computing passband-integrated coefficients per order, following standard practice in low-resolution transit spectroscopy or photometry (Howarth 2011). We derived these theoretical coefficients using the ExoTETHyS software (Morello et al. 2020a,b), and employed the same PHOENIX NewEra stellar templates adopted in our study.

We also investigated whether photometric limb-darkening coefficients are sub-optimal for this application, as they neglect variations between continuum and spectral lines. Therefore, we attempted simultaneous fitting of u and $v \sin i$. However, this approach proved to be computationally expensive and was critically affected by parameter degeneracies (see Appendix C).

Including limb darkening clearly improves both accuracy and precision, reducing the mean offset and the scatter across spectral orders (Fig. 4). The deviation from the target is reduced by 5–10% (consistent with the decrease in the kernel’s effective width when including limb darkening; see Appendix C), and the uncertainty is nearly halved. The top panel of Fig. 5 provides an overview of the derived $v \sin i$ values across the full range of T_{eff} . Because differences between the tested limb-darkening prescriptions remain below 0.5%, the remaining discrepancies likely originate from the convolution procedure rather than the specific choice of law. Nevertheless, including oversampling and limb darkening consistently improves the precision of $v \sin i$ (see Appendix D), which motivates our adoption of the linear law.

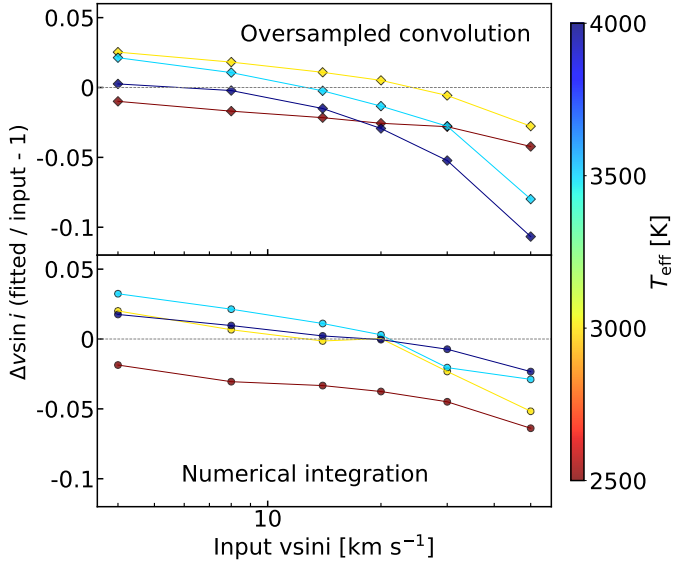


Fig. 5. Normalised difference between input and fitted $v \sin i$ as a function of input $v \sin i$ and a spectrum’s T_{eff} , for oversampled convolution (top panel) and numerical integration (bottom panel).

3.4. Numerical integration

Carvalho & Johns-Krull (2023) developed a method to broaden spectra due to projected rotation by incorporating linear limb darkening via direct numerical integration. We find that this approach is more accurate and precise than convolution, but at a substantially higher computational cost.

The top panel of Fig. 5 shows the derived normalised $v \sin i$ as a function of the input values for different T_{eff} using the oversampled convolution. At high $v \sin i$ ($\gtrsim 20 \text{ km s}^{-1}$), the fitted values increasingly deviate from the input, with the effect being more pronounced at higher T_{eff} , particularly at 4000 K.

The bottom panel of Fig. 5 shows the results obtained using numerical integration. This method is particularly more precise for hotter ($T_{\text{eff}} = 3500\text{--}4000 \text{ K}$) and faster-rotating ($v \sin i \gtrsim 30 \text{ km s}^{-1}$) M dwarfs, and improves precision by up to 5–10%. We recommend numerical integration for individual, star-by-star analyses, whereas convolution remains preferable for statistical studies of large stellar samples.

3.5. Implementation in *serval* with CARMENES spectra

The *serval* pipeline (Zechmeister et al. 2018) was originally developed to compute RVs for exoplanet searches, but it also provides additional data products, including activity indicators and $v \sin i$. We adapted our method to operate within the *serval* framework, following a regression-based approach that is analogous to cross-correlation techniques (Delfosse et al. 1998; Browning et al. 2010; Jeffers et al. 2018).

Based on previous findings (Sect. 3), we applied an oversampled convolution (factor = 5) with a linear limb-darkening kernel, using coefficients computed for each stellar temperature and spectral order, to broaden and resample the reference spectrum. Each co-added target spectrum is compared to the corresponding template order via χ^2 minimisation over a grid of $v \sin i$ values ($0\text{--}150 \text{ km s}^{-1}$, 0.5 km s^{-1} steps) that are applied independently to each spectral order. For slow rotators ($v \sin i < 4 \text{ km s}^{-1}$), a finer velocity grid ($0\text{--}6 \text{ km s}^{-1}$, 0.05 km s^{-1} steps) was used to improve the resolution near 0 km s^{-1} . We took the final $v \sin i$

Table 1. Stars used as templates for computing $v \sin i$ depending on spectral type (Schöfer et al. 2019).

Karmn	GJ identifier	Spectral type	T_{eff} (K)
J14257+236W	GJ 548A	M0.0 V	3850
J18580+059	GJ 740	M0.5 V	3800
J18051–030	GJ 701	M1.0 V	3680
J16254+543	GJ 625	M1.5 V	3600
J06103+821	GJ 226	M2.0 V	3550
J17198+417	GJ 671	M2.5 V	3450
J15194–077	GJ 581	M3.0 V	3400
J17578+046	GJ 699	M3.5 V	3250
J11477+008	GJ 447	M4.0 V	3200
J19216+208	GJ 1235	M4.5 V	3100
J03133+047	GJ 1057	M5.0 V	3050
J00067–075	GJ 1002	M5.5 V	3000
J07403–174	GJ 283B	M6.0 V	2800
J02530+168	GJ 10393	M6.5–9.0 V	2700–2450

as the median of the order-by-order estimates, with the standard deviation providing the uncertainty.

We chose the templates according to the target’s sub-spectral type (Table 1), following Schöfer et al. (2019), who identified the least active and slowest rotator for each sub-type. For M6.5 V and later, Teegarden’s star (J02530+168) was adopted as the reference. All templates were generated with *serval*, which ensured a consistent instrumental profile across all spectral orders. The numerical integration method by Carvalho & Johns-Krull (2023) has been implemented as an alternative alongside convolution.

4. Results

Using CARMENES-VIS spectra of 392 M dwarfs, we present a catalogue of projected rotational velocities that incorporates limb-darkening effects (Table 2). The CARMENES spectra are intrinsically broadened by the instrument, corresponding to an effective $v \sin i = 2 \text{ km s}^{-1}$ (Reiners et al. 2018). Consequently, only an upper limit of 2 km s^{-1} can be placed on stars rotating more slowly than this threshold. Extension to the near infrared is deferred to future work; see Appendix A for a preliminary assessment of its feasibility and potential advantages.

To balance accuracy and computational efficiency, we did not always use all available spectra for each target. For stars with fewer than 20 spectra, all were included; otherwise, we selected 20 evenly spaced spectra. This selection follows the behaviour of the underlying *serval*-inherited function. We verified that using more than 20 spectra does not significantly improve the precision of the derived $v \sin i$.

The command-line input files used to run *serval* are provided in our GitHub repository. Template stars have projected rotational velocities below the instrumental resolution and thus have $v \sin i < 2 \text{ km s}^{-1}$ (see Table 1). In some cases, adjustments were necessary; for example, for certain M3.5 V stars it is preferable to use J14310–122 as the template rather than J17578+046. For stars later than M6.0 V, only the reddest orders (orders 88–66, 688.8–934.3 nm) are used due to low signal-to-noise in the bluer orders.

Theoretical linear limb-darkening coefficients were computed for each spectral order at $T_{\text{eff}} = 2500, 3000, 3500$, and 4000 K and assuming solar metallicity. These coefficients are available in the associated GitHub repository. For intermediate

Table 2. Catalogue of $v \sin i$ values for 392 M-dwarf stars of the CARMENES sample using VIS spectra ^a.

Karmn	Name	Adopted $v \sin i$ (km s ⁻¹)	$v \sin i$ OC (km s ⁻¹)	$v \sin i$ NI (km s ⁻¹)	$v \sin i$ literature (km s ⁻¹)	Ref. ^b	v_{eq} (km s ⁻¹)
J00051+457	BD+44 4548	<2	2	2	2	Rein18	1.61 ± 0.01
J01019+541	G 218–020	29.3 ± 0.9	29.3 ± 0.92	29.2 ± 0.9	30.6 ± 3.06	Rein18	28.2 ± 0.26
J01056+284	GJ 1029	<2	2	2	4.1 ± 0.41	Jen09	0.65 ± 0.02
J02002+130	TZ Ari	<2	2	2	2	Rein18	4.04 ± 0.08
J02164+135	LP 469–206	13.4 ± 0.7	13.4 ± 0.7	13.4 ± 0.7	12.4 ± 1.24	Barn14	...

Notes. ^(a) Only five rows are shown as an example, the complete table is available in the GitHub repository. Listed are: star's Karmn identifier, most common or discovery name, adopted $v \sin i$, $v \sin i$ obtained using oversampled convolution (OC), numerical integration (NI), the value from the literature and reference to the work, and the equatorial rotation velocity. ^(b) Jen09: Jenkins et al. (2009), Barn14: Barnes et al. (2014), Rein18: Reiners et al. (2018).

temperatures, the coefficients were computed via linear interpolation in `serval`.

The stellar temperatures were obtained from Carmencita (Caballero et al. 2017), which gathers values from several works (Soto et al. 2021; Palle et al. 2020; Cifuentes et al. 2020; Marfil et al. 2021). Carmencita is the 'CARMEN(ES) Cool dwarf Information and daTa Archive', and contains a large number of parameters for more than 2000 M dwarfs in the solar neighbourhood that are brighter than $J = 11.5$ mag.

4.1. Oversampled convolution

We compared the 392 $v \sin i$ values derived in this work with literature measurements compiled in Carmencita, and adopted updated values from Reiners et al. (2022) where available (see Table 2). The adopted $v \sin i$ is the value we found to be the most reliable one among our results, using oversampled convolution (OC) and numerical integration (NI), the literature, and the cross check with the equatorial velocity (v_{eq}). A comparison with other works (Passegger et al. 2020; Mas-Buitrago et al. 2024) is discussed in Appendix E.

Most of the derived $v \sin i$ values lie below the instrumental resolution limit of CARMENES (2 km s⁻¹), in agreement with their literature values (see Table 2). The exiting outliers can be seen in Fig. 6; they are those points that deviate from the 1:1 diagonal line. Our $v \sin i$ measurements are also generally in good agreement with the literature above 2 km s⁻¹, with a small number of outliers. The discrepancies are mainly due to either underestimated or overestimated values in previous studies, or to unresolved multiple systems affecting the observed spectra, which make the derived $v \sin i$ unreliable.

Close to the resolution limit, we find some discrepancies with values reported in the literature. Three of our targets (J01339–176, J04376+528, and J09144+526) show $v \sin i$ measurements that are very near the 2 km s⁻¹ limit and that differ from that threshold by less than 0.25 km s⁻¹. Of the remaining three objects, J05365+113 and J19346+045 exhibit $v \sin i > 2 \text{ km s}^{-1} > v_{\text{eq}}$, so only upper limits can be assigned. For J13450+176, our value agrees with that reported by Reiners et al. (2018), but not with the measurement of Reiners et al. (2022).

In Fig. 7, we compare our $v \sin i$ measurements from the oversampled convolution with limb darkening to the equatorial velocities v_{eq} , computed as $v_{\text{eq}} = 2\pi R_{\star}/P_{\text{rot}}$ for stars with available R_{\star} and P_{rot} . Errors in the rotational periods were calculated following Eq. (4) of Shan et al. (2024), and uncertainties in v_{eq} were propagated accordingly. Stars for which $v \sin i > v_{\text{eq}}$ are highlighted in orange and listed in Table 3.

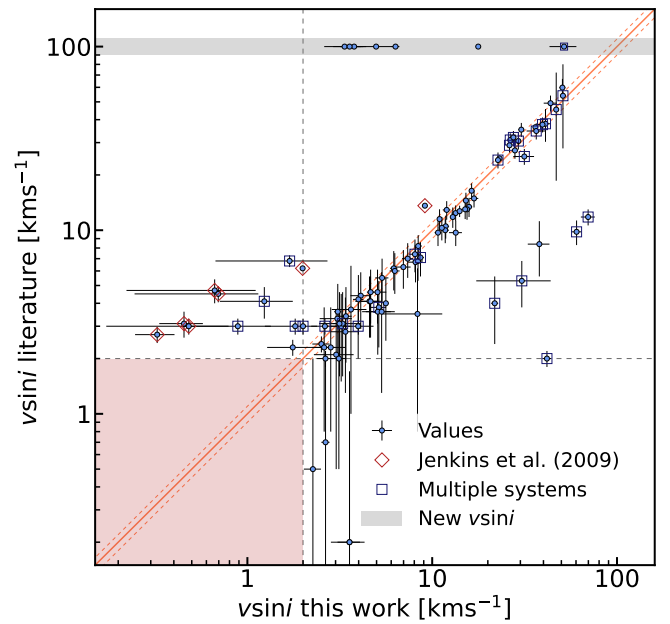


Fig. 6. $v \sin i$ values obtained in this work using the oversampled convolution method compared with literature measurements. Newly determined $v \sin i$ values not previously available are shown in the shaded area at $v \sin i$ (literature) = 100 km s⁻¹. The solid line indicates the 1:1 relation, while the dashed lines correspond to a 10% deviation. Dashed grey lines and the shaded area mark the 2 km s⁻¹ limit of CARMENES. Values inside this region are not plotted.

We revised these outliers and identified six young candidates (J01339–176, J05366+112, J09144+526, J11026+219, J11476+002, and J23548+385) as classified in Cortés-Contreras et al. (2024) based on their kinematics and activity indicators (measured from rotation, X rays, ultraviolet, and H-alpha emission). These targets are highlighted with red diamonds in Fig. 7. According to this study, all of them are fast rotators for their spectral types and all but J05366+112 present X rays luminosities and (NUV-J) levels above the defined threshold for active stars. In addition, they present significant H-alpha emission with the exception of J09144+526, which instead has a lithium measurement (Bischoff et al. 2020). In particular, J11476+002 and J23548+385 are candidates for the IC2391 and UMa groups, as they both have intense magnetic fields measured in Reiners et al. (2022).

Among the remaining outliers, two of them have a doubtful youth assignment in the cited work: J04376+528 and

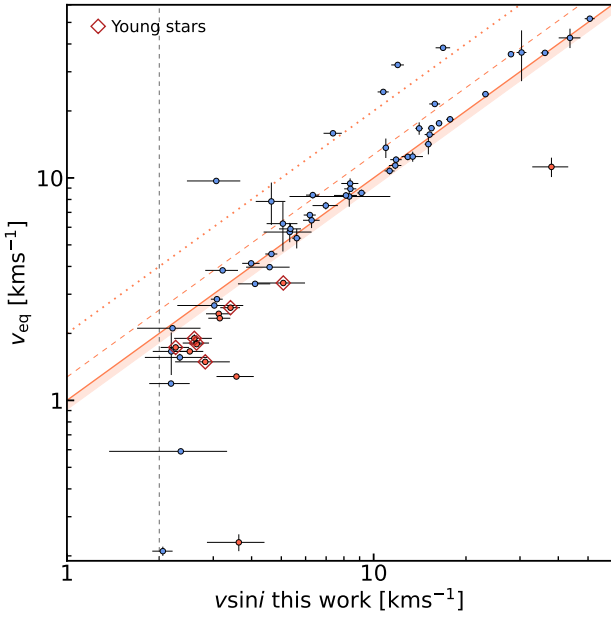


Fig. 7. Values of $v \sin i$ derived from the oversampled convolution method compared to v_{eq} . The linear $1:\frac{4}{\pi}$ relation (dashed line) represents the expected value of $\sin i$ for an isotropic distribution of inclination angles (see Appendix B of [Ruh et al. 2024](#)). The 1:1 relation with a 10% margin (solid line and shaded region) and the $1:\frac{1}{2}$ relation (dotted line) correspond to $i = 90^\circ$ and $i = 30^\circ$, respectively. The vertical dashed grey line indicates the 2 km s^{-1} threshold, and the diamond markers correspond to young candidates ([Cortés-Contreras et al. 2024](#)).

J05365+113. Both are kinematically young (Hyades or galactic young disc) and only a slightly faster rotation compared to others. Another one (J19346+045) is a field star with a rotation period of 8.04 d ([Díez Alonso et al. 2019](#)), and evidence of chromospheric activity (NUV-J and H-alpha emission). J07361–031 is a SB1 binary ([Poveda et al. 2009](#)) in a quadruple system. Finally, J19346+045, J08536–034, and J19169+051S present no relevant information regarding youth or activity.

We report 36 new $v \sin i$ measurements that were not previously available. In Fig. 6, these are represented in the grey shaded region at $v \sin i_{\text{literature}} = 100 \text{ km s}^{-1}$. All values appear reliable except for J10182–204, which is a multiple system where $v \sin i$ is significantly higher than v_{eq} . Because $v_{\text{eq}} < 2 \text{ km s}^{-1}$, an upper limit of 2 km s^{-1} can be adopted for this target.

In total, 21 $v \sin i$ measurements in our sample are considered unreliable. Table 3 summarises the reasons for their unreliability and provides recommended values. For most of these stars, an upper limit can be imposed based on v_{eq} , while in the remaining cases the literature $v \sin i$ is deemed more reliable and is adopted as the preferred value. Out of the 33 multiple systems in our sample identified by [Cifuentes et al. \(2025\)](#), 11 show discrepancies between our measurements and literature values. Seven of these are considered unreliable in our work and are listed in Table 3 as close.

Among the remaining systems, J01056+284, J14155+046, and J15412+759 have $v \sin i > v_{\text{eq}}$ in the literature, whereas our values are consistent, being below 2 km s^{-1} . J05532+242 lacks a measured v_{eq} , but [Jeffers et al. \(2018\)](#) imposed an upper limit of 3 km s^{-1} ; we adopt 2 km s^{-1} . For J14155+046, our measured $v \sin i$ is below 2 km s^{-1} , and the spectrum is more consistent with a slow rotator than with the higher literature value of 6.8 km s^{-1} (see Appendix F).

Table 3. Targets with unreliable $v \sin i$ values.

Karmn	$v \sin i$ (km s^{-1})	Ref. ^a	Comments ^b
J00162+198W	<2	Rein22	Close
J01339–176	<2	This work	$v \sin i > v_{\text{eq}}$
J04376+528	<2	This work	$v \sin i > v_{\text{eq}}$
J05337+019	9.8 ± 1.0	Rein18	Close
J05365+113	<2	Rein22	$v \sin i > v_{\text{eq}}$
J05366+112	$\leq v_{\text{eq}}$	This work	$v \sin i > v_{\text{eq}}$
J05394+406	5.3 ± 0.5	Rein22	Close
J07033+346	<2	This work	$v \sin i > v_{\text{eq}}$
J07361–031	$\leq v_{\text{eq}}$	This work	Close
J08536–034	8.4 ± 0.8	Rein22	$v \sin i > v_{\text{eq}}$
J09144+526	<2	This work	$v \sin i > v_{\text{eq}}$
J10182–204	<2	This work	$v \sin i > v_{\text{eq}}$
J11026+219	<2	This work	$v \sin i > v_{\text{eq}}$
J11055+435	<2	Rein18	$v \sin i > v_{\text{eq}}$
J11476+002	<2	This work	$v \sin i > v_{\text{eq}}$
J16343+571	10.22 ± 1.02	Mor09	Close
J19169+051S	<2	This work	$v \sin i > v_{\text{eq}}$
J19346+045	<2	Rein18	$v \sin i > v_{\text{eq}}$
J20198+229	11.8 ± 1.2	Jen09	Close
J23548+385	3.6 ± 0.4	Rein18	$v \sin i > v_{\text{eq}}$
J23585+076	<2	Rein18	Close

Notes. ^(a) Jen09: [Jenkins et al. \(2009\)](#), Mor09: [Morales et al. \(2009\)](#), Rein18: [Reiners et al. \(2018\)](#), Rein22: [Reiners et al. \(2022\)](#). ^(b) Comments indicate why they are unreliable. Close systems are identified by [Cifuentes et al. \(2025\)](#).

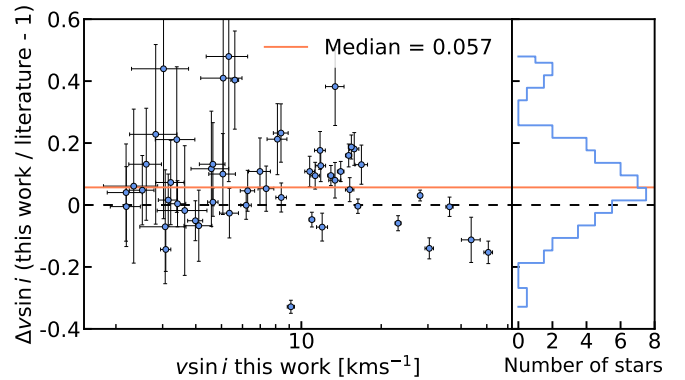


Fig. 8. Histogram of the normalised difference between the $v \sin i$ value ($> 2 \text{ km s}^{-1}$) computed with oversampled convolution and the literature, excluding the outliers. The median is marked with a horizontal solid line.

We identified seven $v \sin i$ measurements from [Jenkins et al. \(2009\)](#) that are not in agreement with our results (red diamonds in Fig. 6): J02022+103, J02465+164, J03090+100, J14578+566, J15100+193, J15238+174, and J20305+654. For three of these targets, the values from the cited work exceed v_{eq} , whereas our $v \sin i$ measurements are consistent. The remaining targets have $v \sin i < 2 \text{ km s}^{-1}$ in our analysis and their spectra are better matched by a slowly rotating template than by a broadened one. We therefore recommend adopting our values as updated measurements for these stars.

Excluding outliers and considering only $v \sin i > 2 \text{ km s}^{-1}$, our measurements are systematically higher than literature values by a median of 5.7%, as illustrated in Fig. 8. An increase

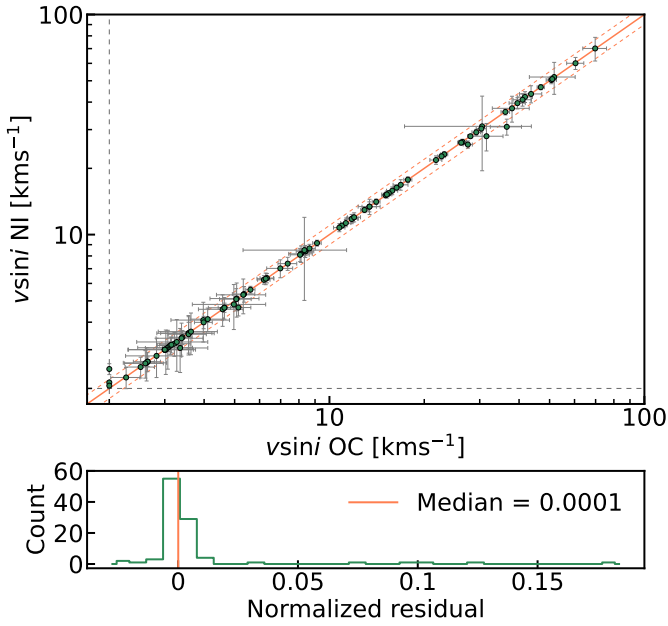


Fig. 9. Top panel: comparison between $v \sin i$ computed with numerical integration and oversampled convolution. Dashed lines represent the 2 km s^{-1} limit and diagonal lines mark the 1:1 relation $\pm 10\%$. Bottom panel: histogram of the normalised residuals with respect to the 1:1 relation for $v \sin i > 2 \text{ km s}^{-1}$. Median value are represented by a vertical line.

up to 10% was expected due to the inclusion of limb darkening (depending on the T_{eff} and $v \sin i$; see Sect. 3.3 and Appendix C). At high rotation rates ($v \sin i \gtrsim 20 \text{ km s}^{-1}$), values may be slightly underestimated owing to the intrinsic limitations of the oversampled convolution method (see Fig. 5). The median relative uncertainty of our $v \sin i$ values above 2 km s^{-1} is 6.8%, compared to 15.4% for the literature.

4.2. Numerical integration

The OC method is approximately 3.5 times faster than the NI approach, although the latter is expected to yield higher precision (see Sect. 3.4). Table 2 lists all $v \sin i$ values obtained with both methods, while Fig. 9 compares their results, which show excellent agreement. The histogram of the normalised residuals displays a median difference of only 0.1%, which is smaller than the offsets predicted from synthetic data in Sect. 3.4, where differences of about 1–2% were found for slow and intermediate rotators, and up to 5–10% for the fastest rotators (see Fig. 5).

Overall, values below and above 2 km s^{-1} are fully consistent between methods. The substantial increase in computational time relative to the modest gain in precision does not justify using NI instead of OC, particularly for statistical studies or slow-to-moderate rotators ($v \sin i < 20 \text{ km s}^{-1}$). As discussed in Sect. 3.4, the improvement from NI only becomes noticeable for faster rotators ($30\text{--}50 \text{ km s}^{-1}$) and hotter stars ($T_{\text{eff}} = 4000 \text{ K}$). However, this effect remains minor for the CARMENES sample, yielding a similar median error to the OC method of 6.5%.

5. Conclusions

We present a novel method to determine the projected rotational velocity ($v \sin i$) of stars from CARMENES-VIS spectra. This approach upgrades the `serval` pipeline by (i) adopting an

order-dependent rotational broadening kernel that accounts for wavelength- and temperature-dependent stellar limb darkening, and (ii) performing spectral oversampling prior to convolution with the template spectrum. The effectiveness of these improvements has been tested using both synthetic and real datasets.

By applying this method, we derived a homogeneous catalogue of $v \sin i$ measurements for 392 M dwarfs observed with CARMENES-VIS. Our results show overall good agreement with previously published values, while achieving a substantially higher precision. The median relative uncertainty of our measurements is 6.8%, compared to 15.4% for literature values. Additionally, we report 36 new $v \sin i$ measurements that were not previously available. This catalogue provides a robust and homogeneous reference for studies of stellar rotation in low-mass stars and will be particularly valuable for the characterisation of M-dwarf planetary systems, including applications to age estimates, radial-velocity surveys, and spin-orbit investigations.

Data availability

Our pipeline, data, and results are available in a GitHub repository at <https://github.com/rvarasg/vsini-limb-darkening>. The full Table 2 is available at the CDS via <https://cdsarc.cds.unistra.fr/viz-bin/cat/J/A+A/709/A244>. The CARMENES DR1 dataset, which includes most of the spectra used in this work, is publicly available at <https://carmenes.cab.inta-csic.es>.

Acknowledgements. CARMENES is an instrument at the Centro Astronómico Hispano en Andalucía (CAHA) at Calar Alto (Almería, Spain), operated jointly by the Junta de Andalucía and the Instituto de Astrofísica de Andalucía (CSIC). Funding for CARMENES has been provided by the Max-Planck-Institut für Astronomie (MPIA), Consejo Superior de Investigaciones Científicas (CSIC), European Regional Development Fund (ERDF), Ministerio de Ciencia, Innovación y Universidades (MICIU), Deutsche Forschungsgemeinschaft (DFG), and the members of the CARMENES Consortium (<https://carmenes.caha.es>). This publication was based on observations collected under the CARMENES Legacy-Plus project. The authors wish to express their sincere thanks to all members of the Calar Alto staff for their expert support of the instrument and telescope operation. We used data from the CARMENES data archive at CAB (CSIC-INTA). We acknowledge financial support from the Agencia Estatal de Investigación (AEI/10.13039/501100011033) of the MICIU and the ERDF “A way of making Europe” through projects PID2022-137241NB-C41-I-41, PID2021-125627OB-C31-I-21, PID2019-109522GB-C52, RYC2022-037854-I, and RYC2021-031640-I (2023AT003), and from the Centre of Excellence “Severo Ochoa” and “María de Maeztu” awards to the Instituto de Astrofísica de Andalucía (CEX2021-001131-S) and Institut de Ciències de l’Espai (CEX2020-001058-M). We also acknowledge financial support from the project AST22_00001_8 of the Junta de Andalucía and the Ministerio de Ciencia, Innovación y Universidades funded by the NextGenerationEU and the Plan de Recuperación, Transformación y Resiliencia.

References

- Barnes, J. R., Jenkins, J. S., Jones, H. R. A., et al. 2014, *MNRAS*, **439**, 3094
- Baroch, D., Morales, J. C., Ribas, I., et al. 2020, *A&A*, **641**, A69
- Bischoff, R., Mugrauer, M., Torres, G., et al. 2020, *Astron. Nachr.*, **341**, 908
- Bonfils, X., Delfosse, X., Udry, S., et al. 2013, *A&A*, **549**, A109
- Browning, M. K., Basri, G., Marcy, G. W., West, A. A., & Zhang, J. 2010, *AJ*, **139**, 504
- Caballero, J. A., Guàrdia, J., López del Fresno, M., et al. 2016, *SPIE Conf. Ser.*, **9910**, 99100E
- Caballero, J. A., Cortés-Contreras, M., Alonso-Floriano, F. J., et al. 2017, in *Highlights on Spanish Astrophysics IX*, eds. S. Arribas, A. Alonso-Herrero, F. Figueras, C. Hernández-Monteagudo, A. Sánchez-Lavega, & S. Pérez-Hoyos, 496
- Canocchi, G., Morello, G., Lind, K., et al. 2024, *A&A*, **692**, A43
- Carvalho, A., & Johns-Krull, C. M. 2023, *RNAAS*, **7**, 91

- Cifuentes, C., Caballero, J. A., Cortés-Contreras, M., et al. 2020, *A&A*, **642**, A115
- Cifuentes, C., Caballero, J. A., González-Payo, J., et al. 2025, *A&A*, **693**, A228
- Claret, A. 2000, *A&A*, **363**, 1081
- Claret, A., Hauschildt, P. H., & Torres, G. 2025, *A&A*, **699**, A97
- Cortés-Contreras, M., Caballero, J. A., Montes, D., et al. 2024, *A&A*, **692**, A206
- Delfosse, X., Forveille, T., Perrier, C., & Mayor, M. 1998, *A&A*, **331**, 581
- Díaz-Cordoves, J., & Gimenez, A. 1992, *A&A*, **259**, 227
- Díez Alonso, E., Caballero, J. A., Montes, D., et al. 2019, *A&A*, **621**, A126
- Fuhrmeister, B., Czesla, S., Schmitt, J. H. M. M., et al. 2018, *A&A*, **615**, A14
- Fuhrmeister, B., Czesla, S., Perdelwitz, V., et al. 2023, *A&A*, **670**, A71
- Gray, D. F. 2005, *The Observation and Analysis of Stellar Photospheres*, 3rd edn. (Cambridge University Press)
- Hauschildt, P. H., Barman, T., Baron, E., Aufdenberg, J. P., & Schweitzer, A. 2025, *A&A*, **698**, A47
- Henry, T. J., & Jao, W.-C. 2024, *ARA&A*, **62**, 593
- Henry, T. J., Jao, W.-C., Subasavage, J. P., et al. 2006, *AJ*, **132**, 2360
- Henry, T. J., Jao, W.-C., Winters, J. G., et al. 2018, *AJ*, **155**, 265
- Hestroffer, D. 1997, *A&A*, **327**, 199
- Howarth, I. D. 2011, *MNRAS*, **418**, 1165
- Jeffers, S. V., Schöfer, P., Lamert, A., et al. 2018, *A&A*, **614**, A76
- Jeffers, S. V., Barnes, J. R., Schöfer, P., et al. 2022, *A&A*, **663**, A27
- Jenkins, J. S., Ramsey, L. W., Jones, H. R. A., et al. 2009, *ApJ*, **704**, 975
- Kopal, Z. 1950, *Harvard College Observ. Circ.*, **454**, 1
- Marfil, E., Tabernero, H. M., Montes, D., et al. 2021, *A&A*, **656**, A162
- Mas-Buitrago, P., González-Marcos, A., Solano, E., et al. 2024, *A&A*, **687**, A205
- Milne, E. A. 1921, *MNRAS*, **81**, 361
- Morales, J. C., Ribas, I., Jordi, C., et al. 2009, *ApJ*, **691**, 1400
- Morello, G., Tsiaras, A., Howarth, I. D., & Homeier, D. 2017, *AJ*, **154**, 111
- Morello, G., Claret, A., Martin-Lagarde, M., et al. 2020a, *J. Open Source Softw.*, **5**, 1834
- Morello, G., Claret, A., Martin-Lagarde, M., et al. 2020b, *AJ*, **159**, 75
- Morello, G., Casasayas-Barris, N., Orell-Miquel, J., et al. 2022, *A&A*, **657**, A97
- Newton, E. R., Irwin, J., Charbonneau, D., et al. 2016, *ApJ*, **821**, 93
- Palle, E., Nortmann, L., Casasayas-Barris, N., et al. 2020, *A&A*, **638**, A61
- Passegger, V. M., Bello-García, A., Ordieres-Meré, J., et al. 2020, *A&A*, **642**, A22
- Poveda, A., Allen, C., Costero, R., Echevarría, J., & Hernández-Alcántara, A. 2009, *ApJ*, **706**, 343
- Quirrenbach, A., Amado, P. J., Caballero, J. A., et al. 2014, *SPIE Conf. Ser.*, **9147**, 91471F
- Quirrenbach, A., Amado, P. J., Ribas, I., et al. 2018, *SPIE Conf. Ser.*, **10702**, 107020W
- Reiners, A., Joshi, N., & Goldman, B. 2012, *AJ*, **143**, 93
- Reiners, A., Zechmeister, M., Caballero, J. A., et al. 2018, *A&A*, **612**, A49
- Reiners, A., Shulyak, D., Käpylä, P. J., et al. 2022, *A&A*, **662**, A41
- Ribas, I., Reiners, A., Zechmeister, M., et al. 2023, *A&A*, **670**, A139
- Ruh, H. L., Zechmeister, M., Reiners, A., et al. 2024, *A&A*, **692**, A138
- Sabotta, S., Schlecker, M., Chaturvedi, P., et al. 2021, *A&A*, **653**, A114
- Schöfer, P., Jeffers, S. V., Reiners, A., et al. 2019, *A&A*, **623**, A44
- Shan, Y., Revilla, D., Skrzypinski, S. L., et al. 2024, *A&A*, **684**, A9
- Soto, M. G., Anglada-Escudé, G., Dreizler, S., et al. 2021, *A&A*, **649**, A144
- Suárez Mascareño, A., Rebolo, R., González Hernández, J. I., & Esposito, M. 2015, *MNRAS*, **452**, 2745
- Zechmeister, M., Reiners, A., Amado, P. J., et al. 2018, *A&A*, **609**, A12

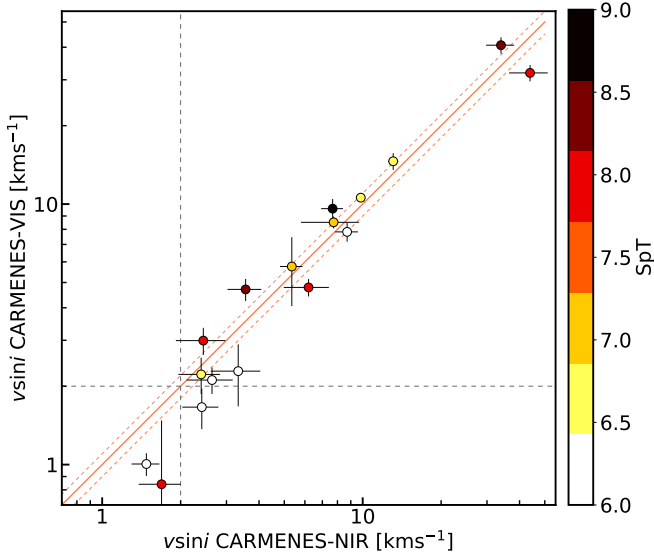


Fig. A.1: Comparison of $v \sin i$ derived from CARMENES-VIS and NIR spectra for M dwarfs later than M6.0 V. No oversampling or limb-darkening was applied. Lines indicate the 1:1 relation ($\pm 10\%$) and the 2 km s^{-1} limit.

Appendix A: $v \sin i$ using near-infrared spectra

We analysed $v \sin i$ using both CARMENES-NIR and VIS spectra for the coldest stars in the sample (16 objects). This selection is motivated by their higher near-infrared S/N relative to hotter stars, comparable to the VIS S/N (Reiners et al. 2018). J07403-174 and J02530+168 were used as templates (Table 1), and their $v \sin i$ values are not computed here. For this preliminary analysis, we did not apply oversampling nor include limb-darkening.

Figure A.1 presents the comparison of $v \sin i$ derived from NIR and VIS spectra for this subsample. Most measurements are consistent between the two datasets, with a few cases close to or below the 2 km s^{-1} limit. A more detailed analysis, analogous to that performed for the VIS data in this study, is required to fully characterise the small remaining differences between the NIR and VIS results.

Appendix B: Rotation kernel with limb-darkening

Following Gray (2005), the disc-integrated spectrum of a rigidly rotating, spherical star can be written as a convolution:

$$F(v) = \int_{-v \sin i}^{+v \sin i} S(v-v') \tilde{K}(v') dv', \quad (\text{B.1})$$

where $S(v)$ is the intrinsic, non-rotating stellar spectrum, and

$$v = c \frac{\lambda - \lambda_{\text{ref}}}{\lambda_{\text{ref}}} \quad (\text{B.2})$$

is the Doppler velocity relative to a reference wavelength. The kernel $\tilde{K}(v')$ represents the relative contribution of all surface elements sharing the same projected line-of-sight velocity v' . Choosing the x -axis along the projected stellar equator, the line-of-sight velocity of a surface element is

$$v'(x) = (v \sin i) x, \quad -1 \leq x \leq 1, \quad (\text{B.3})$$

in normalised Cartesian coordinates on the projected stellar disc. Each value of v' therefore corresponds to a chord across

the stellar disc perpendicular to the projected equator. The unnormalised kernel is obtained by integrating the surface intensity along these chords,

$$K(x) = \int_{-a}^a I(x, y) dy, \quad a = \sqrt{1-x^2}. \quad (\text{B.4})$$

We assume radial limb-darkening, so that $I(x, y) = I(\mu)$ with $\mu = \sqrt{1-x^2-y^2}$. Most commonly used limb-darkening laws can be written as linear combinations of powers of μ :

$$I(\mu) = \sum_{\gamma} c_{\gamma} \mu^{\gamma}. \quad (\text{B.5})$$

Replacing the above intensity profile into Eq. (B.4), the kernel becomes

$$K(x) = \sum_{\gamma} c_{\gamma} \int_{-a}^a (a^2 - y^2)^{\frac{\gamma}{2}} dy, \quad a = \sqrt{1-x^2}. \quad (\text{B.6})$$

Applying the substitution $y = a \cos t$,

$$K(x) = \sum_{\gamma} c_{\gamma} a^{\gamma+1} \int_0^{\pi} (\sin t)^{\gamma+1} dt, \quad a = \sqrt{1-x^2}. \quad (\text{B.7})$$

In absence of limb-darkening, there is only one term with $\gamma = 0$ ($c_0 = 1$), so

$$K_{\text{unif}}(x) = 2 \sqrt{1-x^2}. \quad (\text{B.8})$$

The linear limb-darkening law coincides with Eq. (B.5) for $c_0 = 1-u$ and $c_1 = u$. The corresponding un-normalised kernel is

$$K_{\text{lin}}(x) = 2(1-u) \sqrt{1-x^2} + \frac{\pi}{2} u (1-x^2). \quad (\text{B.9})$$

The kernel for the quadratic law is obtained with $c_0 = 1-u_1-u_2$, $c_1 = u_1+2u_2$ and $c_2 = -u_2$:

$$K_{\text{quad}}(x) = 2(1-u_1-u_2) \sqrt{1-x^2} + \frac{\pi}{2} (u_1+2u_2)(1-x^2) - \frac{4}{3} u_2 (1-x^2)^{\frac{3}{2}}. \quad (\text{B.10})$$

The integrals for non-integer γ exponents do not admit a closed-form analytical solution. They can, however, be expressed in terms of the Γ function:

$$\int_0^{\pi} (\sin t)^{\gamma+1} dt = \pi \frac{\Gamma(\frac{\gamma+2}{2})}{\Gamma(\frac{\gamma+3}{2})}, \quad \gamma > -2. \quad (\text{B.11})$$

By combining Eqs. (B.6) and (B.11), the broadening kernel can be computed for other limb-darkening laws, including the square-root, power-2, and four-coefficient prescriptions.

Appendix C: Numerical aspects of the rotation kernel

Figure C.1 shows the resulting normalised kernel in Eq. (8) for selected values of the limb-darkening coefficient u . The kernel transitions from a semi-circular profile for $u = 0$ to an increasingly parabolic shape as $u \rightarrow 1$. We derived the effective width of each kernel, σ_u , where σ_u^2 corresponds to the kernel variance including limb-darkening. The ratio σ_u/σ_0 is a measure of the

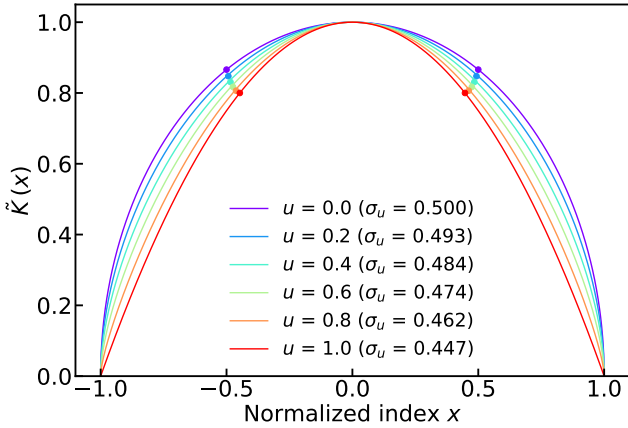


Fig. C.1: Rotational broadening kernel for different limb-darkening coefficients u . Circular markers correspond to the effective width of each kernel.

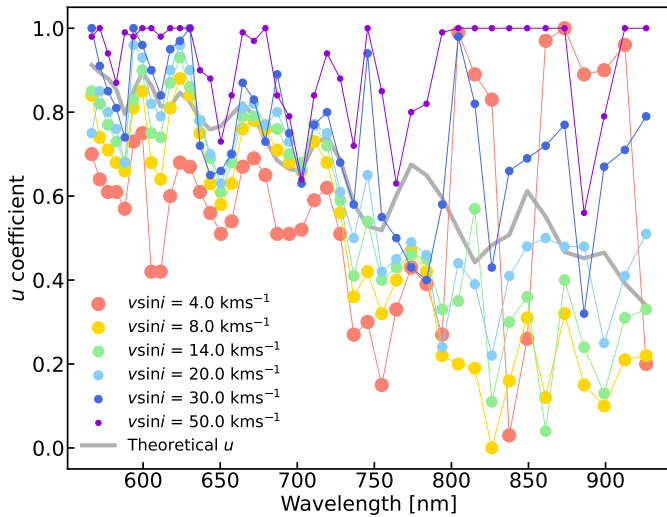


Fig. C.2: Limb-darkening u coefficient as a function of wavelength, when fitting simultaneously with $v \sin i$.

underestimation of $v \sin i$ when limb-darkening is neglected. For instance, $u = 0.6$ leads to an underestimation of approximately 6%. As illustrated by the narrower kernel at higher u , neglecting limb-darkening biases the recovered $v \sin i$ toward lower values.

We attempted to simultaneously fit $v \sin i$ and the limb-darkening coefficient u using the oversampled convolution method, but found notable inconsistencies. The fitted u values vary systematically with the target's $v \sin i$ (see Fig. C.2), and for higher rotational velocities and T_{eff} , where the method becomes less reliable (Sect. 3.4), u tends to converge toward 1 across all spectral orders, attempting to compensate for discrepancies between the input and recovered $v \sin i$. Furthermore, the fitted coefficients show poor agreement with the theoretical predictions.

We examined whether the limitations of the method could arise from an overly simplified treatment of limb-darkening. In the context of exoplanetary transit studies, the most commonly employed laws are linear (Milne 1921), quadratic (Kopal 1950), square-root (Diaz-Cordoves & Gimenez 1992), four-coefficient (Claret 2000), and power-2 (Hestroffer 1997). Figure C.3 shows the differences between the fitted $v \sin i$ values obtained as a function of the target's $v \sin i$, for 4000 K. The discrepancies

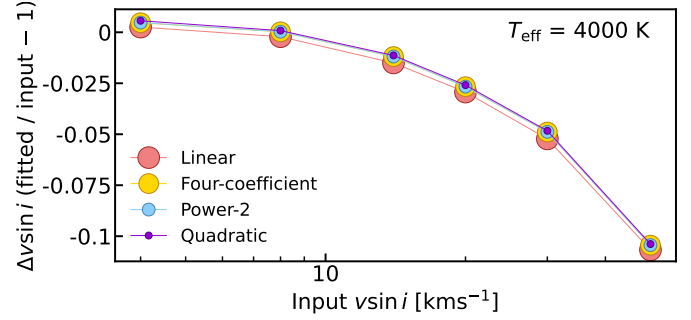


Fig. C.3: Normalized difference between input and fitted $v \sin i$ as a function of the input $v \sin i$ for different limb-darkening laws.

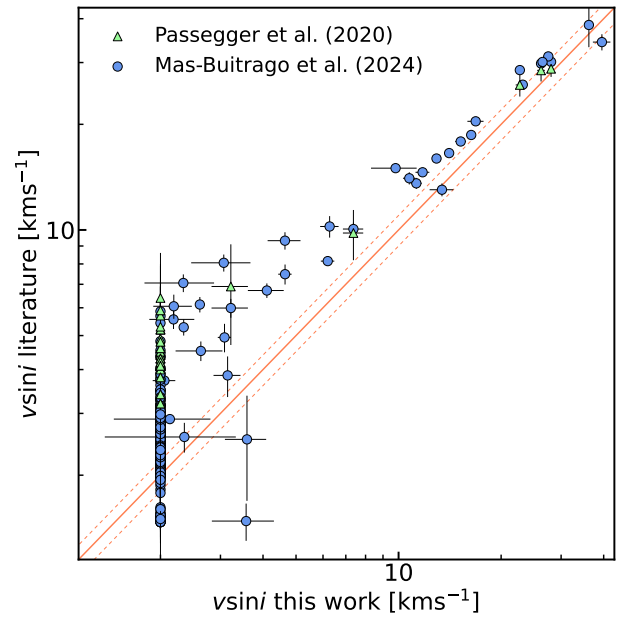


Fig. E.1: Comparison of our $v \sin i$ values with the results from Passegger et al. (2020) and Mas-Buitrago et al. (2024)

among the non-linear models are minimal, remaining below 0.5% even in the most extreme cases when compared to the linear law.

Appendix D: Oversampling and limb-darkening impact during convolution

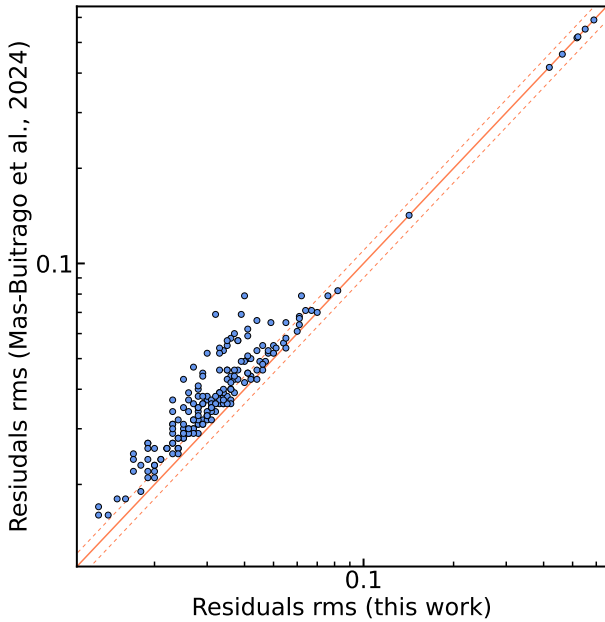
Table D.1 presents the results obtained using regular convolution without limb-darkening (RCWLD) and oversampled convolution with linear limb-darkening (OCLLD) for all combinations of $v \sin i$ and T_{eff} in our spectral sample. In general, the more sophisticated approach yields values closer to the target $v \sin i$ and with smaller uncertainties. The simplest method systematically underestimates the rotational broadening of the target spectrum and, in most cases, does not agree with the target value within the errors.

Appendix E: Comparison with other works

We also compared our catalogue with the results of Passegger et al. (2020) and Mas-Buitrago et al. (2024, see our Fig. E.1), who derived the projected rotational velocities of CARMENES

Table D.1: Derived $v \sin i$ values for all the T_{eff} and target $v \sin i$ combinations, using regular convolution without limb-darkening (RCWLD) and oversampled convolution with linear limb-darkening (OCLLD).

Target $v \sin i$ [km s^{-1}]	Method	$v \sin i$ [km s^{-1}] ($T_{\text{eff}} = 2500 \text{ K}$)	$v \sin i$ [km s^{-1}] ($T_{\text{eff}} = 3000 \text{ K}$)	$v \sin i$ [km s^{-1}] ($T_{\text{eff}} = 3500 \text{ K}$)	$v \sin i$ [km s^{-1}] ($T_{\text{eff}} = 4000 \text{ K}$)
4.0	RCWLD	3.97 ± 0.31	4.08 ± 0.25	4.18 ± 0.22	4.26 ± 0.22
	OCLLD	3.96 ± 0.06	4.1 ± 0.06	4.09 ± 0.07	4.01 ± 0.06
8.0	RCWLD	7.3 ± 0.18	7.77 ± 0.27	7.74 ± 0.21	7.69 ± 0.17
	OCLLD	7.86 ± 0.14	8.15 ± 0.12	8.09 ± 0.13	7.98 ± 0.15
14.0	RCWLD	12.64 ± 0.4	13.2 ± 0.41	13.35 ± 0.3	13.12 ± 0.33
	OCLLD	13.7 ± 0.28	14.15 ± 0.18	13.97 ± 0.28	13.79 ± 0.4
20.0	RCWLD	17.95 ± 0.59	18.79 ± 0.56	18.72 ± 0.5	18.55 ± 0.73
	OCLLD	19.49 ± 0.43	20.1 ± 0.24	19.73 ± 0.59	19.41 ± 0.84
30.0	RCWLD	26.91 ± 0.84	28.07 ± 0.7	27.57 ± 1.36	26.99 ± 1.82
	OCLLD	29.16 ± 0.72	29.83 ± 0.49	29.17 ± 1.6	28.43 ± 2.03
50	RCWLD	44.07 ± 1.81	45.5 ± 1.67	43.72 ± 4.96	42.95 ± 5.43
	OCLLD	47.89 ± 1.7	48.62 ± 1.85	46.01 ± 5.39	44.66 ± 5.91

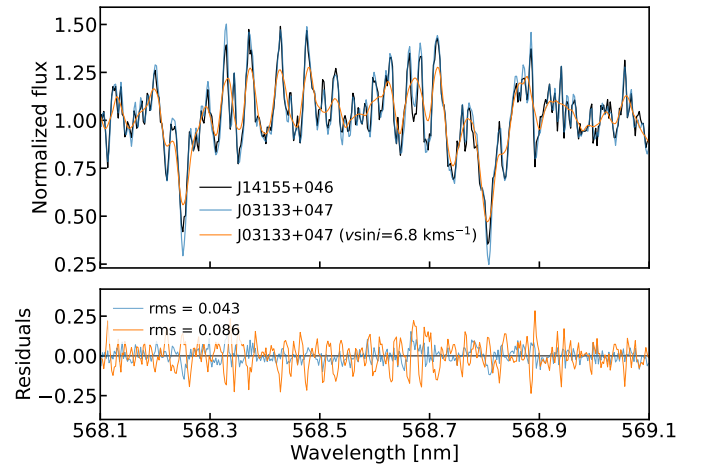

 Fig. E.2: rms of the residuals between target spectrum and template rotationally broadened using both $v \sin i$ from this work and Mas-Buitrago et al. (2024).

targets using deep-learning methods. Their $v \sin i$ values are typically larger, particularly for slow rotators. For $v \sin i$ above 10 km s^{-1} , the differences decrease. Both studies also report systematically higher $v \sin i$ values than those derived by Reiners et al. (2018). Our results lie between these estimates, but are closer to those of Reiners et al. (2018) and Reiners et al. (2022).

For all targets in common with Mas-Buitrago et al. (2024), we compared the stellar spectrum with the corresponding template (see Table 1) rotationally broadened using both sets of $v \sin i$ values. The rms of the residuals is shown in Fig. E.2. In general, our $v \sin i$ measurements yield smaller rms values, particularly for slow rotators. This indicates that our results reproduce the observed broadening of the spectral lines in the CARMENES VIS spectra more accurately.

Appendix F: Spectrum and $v \sin i$ of J14155+046

Jenkins et al. (2009) reported a projected rotational velocity of $v \sin i = 6.8 \text{ km s}^{-1}$ for J14155+046. In our analysis, we obtained a value below 2 km s^{-1} , which corresponds to the lower limit of our method. Comparing the spectrum of J14155+046 with that of J03133+047, a reference star in our sample with $v \sin i < 2 \text{ km s}^{-1}$, we find a better match than when broadening the spectrum of J03133+047 to higher velocities, as the rms of the residuals halve (see Fig. F.1).


 Fig. F.1: Top: Chunk of the CARMENES-VIS co-added spectrum of J14155+046 compared to the spectrum of J03133+047, without and with 6.8 km s^{-1} rotational broadening (Jenkins et al. 2009). Bottom: Residuals with respect to J14155+046.